Role of metal contacts on the electric and thermoelectric response of hBN/WSe 2 based transistors

Salvatore Timpa, Mehrdad Rahimi, Jacko Rastikian, Stéphan Suffit, François Mallet, Philippe Lafarge, Clément Barraud, Maria Luisa Della Rocca

Role of metal contacts on the electric and thermoelectric response of hBN/WSe_2 based transistors

Salvatore Timpa,[1] Mehrdad Rahimi,[1] Jacko Rastikian,[1] Stéphan Suffit,[1] François Mallet,[1] Philippe Lafarge,[1] Clément Barraud,[1] and Maria Luisa Della Rocca[1]

Laboratoire Matériaux et Phénomènes Quantiques, Université de Paris, CNRS, F-75013, Paris, France

(*Electronic mail: maria-luisa.della-rocca@u-paris.fr)

(*Electronic mail: salvatore.timpa@u-paris.fr)

(Dated: 20 February 2022)

Transition metal dichalcogenides represent an emergent platform for energy conversion solutions at the nanoscale. The thermoelectric performances of devices based on two-dimensional materials rely not only on the electric and thermal properties of the used materials, but also on device engineering. In actual devices, hybridization effects at the semiconductor/metal interface strongly affect the local band structure with important consequences on charge injection and thermoelectric response. Here, we investigate the role of different metal contacts (Ag, Pd, Co, Ti) on the electric and thermoelectric properties of hBN-supported few layers WSe_2 transistors. In our devices, we reveal a metal contact-dependent Seebeck response with high values of the Seebeck coefficient (S), up to $\sim$ 180 μV/K, and power factors ($PF = S^2\sigma$) as high as 2.4 μW/cm K^2 (Co), in agreement with the state-of-the-art. Metal electrodes for which weak interface hybridization is theoretically expected (Ag) show the lowest electrical conductivity and the highest Seebeck coefficient. On the opposite, for expected strong interface hybridization (Pd, Co, Ti), electrical conductivity increases and slightly reduced S values are measured. Our work unveils the importance of metal contacts engineering to optimize the thermoelectric performances of actual few layers transition metal dichalcogenides based transistors.

I. INTRODUCTION

Understanding and managing heat at the nanoscale constitutes a major on-going scientific and technological challenge. Thermoelectric (TE) materials[1–3] are solid-state energy converters able to produce electrical work from thermal energy[4–7]. Energy conversion of TE devices is ruled by the figure of merit, ZT, defined as $S^2\sigma T/\kappa$, where S is the Seebeck coefficient (or thermopower), σ and κ are the electrical and thermal conductivities, and T is the absolute temperature. According to Mott formula, the Seebeck coefficient scales with the density of states (DOS) and the derivative of the electrical conductivity. Therefore, low dimensionality, quantum confinement and band structure engineering have opened new routes to improve TE performances[8–11]. In this context, 2D materials and in particular transition metal dicalchogenides (TMDs), such as molybdenum disulfide (MoS_2) and tungsten diselenide (WSe_2), have recently received great attention. In TMDs, the band gap can be modulated by varying the thickness and the charge carriers density is efficiently controlled by a gate voltage[12,13]. MoS_2 has been extensively studied and thermoelectric powers as large as 2 mV/K at low temperature ($\sim$ 50 K) have been experimentally demonstrated[14–16]. Although less studied, WSe_2 has shown maximum S of about $\sim$ 300 μV/K and power factors PF ($PF = S^2\sigma$) of $\sim$ 37 μW/cm K^2 in electrolyte gated transistors[17–19]. Moreover, very low in-plane thermal conductivity (1 - 2 W/mK) has been experimentally reported and theoretically confirmed in this 2D material[20–23], making it particularly appealing for TE applications.

Due to their reduced dimensionality, 2D materials are strongly affected by the environment. Surface charge states in conventional SiO_2 substrates induce scattering and potential disorder in the supported 2D materials[24,25]. Hexagonal boron nitride (hBN) turns out to be an effective solution to this problem, being hBN an atomically flat insulating 2D material with inert and free-of-charge-traps surface[26,27]. The electric and thermoelectric performances of graphene and MoS_2 are significantly enhanced when implementing hBN-supported configurations[28,29]. Making good metal contacts is also a crucial issue for the development of TMDs-based devices. Depending on the electrode nature, n-type, p-type and ambipolar transport have been reported in WSe_2-based transistors[30–33]. Recently Wang et al. have shown that the Schottky barrier height and the band gap at the interface between a metal electrode and monolayer or bilayer WSe_2 strongly depend on the nature of the metal[34]. This is due to the different bonding strength and band hybridization degrees of the different interfaces. Similar conclusions have been theoretically achieved also in the case of $MoSe_2$[35,36]. Since the Seebeck coefficient is expected to depend on the band structure of the TE material, the question arises whether the metal contacts also affect the thermoelectric properties of TMDs.

In this work, we experimentally investigate the electric and thermoelectric response of few layers WSe_2-based transistors fabricated with different metal contacts (Ag, Pd, Co, Ti) and using hBN as supporting layer. We report a metal contact dependent electric and thermoelectric response. The highest Seebeck coefficient, with a maximum value of $\sim$ 180 μV/K, is observed with Ag electrodes, for which the lowest 2-point electrical conductivity is measured, resulting in low power factors, $\sim$ 0.02 μW/cm K^2. When using Co, the Seebeck coefficient reduces to $\sim$ 150 μV/K while the highest power factors is achieved, up to 2.4 μW/cm K^2, due to improved charge injection. These observations are qualitatively coherent with the expected metal/semiconductor interface hy-

bridization variation theoretically predicted for different metal contact interface with monolayer and bilayer WSe_2[34].

II. DEVICES FABRICATION AND MEASUREMENTS

We prepare WSe_2-based transistors starting by the exfoliation of hBN and WSe_2 flakes from bulk crystals (HQ Graphene). A hBN/WSe_2 heterostructure is then stacked by the dry hot pick-up transfer technique[37] on the top of a Au gate electrode on a prefabricated chip. The prefabricated chip is a Si/SiO_2 (280 nm-thick) substrate where a local gate electrode and a nanowire acting as micro-heater (spaced by 150 - 350 nm) are fabricated by standard e-beam lithography and metal deposition (Ti/Au, 5/35 nm). Two metallic nanowires (6 μm-long, 80 nm-thick, 400 nm-wide and spaced by 5 μm), acting simultaneously as local electrodes and thermometers, are successively fabricated on the hBN/WSe_2 heterostructure. The metallic nanowires have been made in Ag (sample 1), Pd (sample 2), Co (sample 3) and Ti (sample 4), all with a Au capping layer to prevent oxidation. All metal evaporation steps are performed at $\sim 10^{-8}$ mbar, after 2 hours of in-vacuum annealing at 120°C to remove possible contaminants[38,39]. The choice of the metal contacts is justified by the electron and hole affinities for few layers WSe_2[40]: high (low) work-function metals, such as Pd and Co (Ag and Ti), allow achieving, in principle, good hole[41,42] (electron[30,39]) injection. Figure 1 (a) shows an optical image of a representative sample.

Schematics of the device with the wiring for electric and thermoelectric measurements are shown in Figure 1 (b) and (c), respectively. Measurements are carried out at room temperature under high vacuum ($P \sim 10^{-7}$ mbar) in a micro probe station (Nextron) after in-situ annealing (at 400°C) improving adhesion between the flakes and electrical contact quality. Since semiconducting devices may reach very large OFF-state resistances, transport measurements are performed in a 2-point configuration by voltage-biasing the samples and probing the current flowing through the WSe_2 channel as a function of the gate voltage by a low-noise current-voltage amplifier. Leakage currents between the heater (as well as the gate) and the source and drain electrodes are lower than the sensitivity of our experimental set-up ($\sim$ 10 pA) in the explored gate and source-drain applied voltages.

Thermoelectric measurements are performed using a DC approach. A DC current (I_{heater}) is injected through the microfabricated metal heater. Due to Joule heating, a temperature gradient ΔT is developed in the longitudinal direction of the device inducing a thermoelectric voltage, V_{TE}. The estimation of ΔT is performed by measuring the resistance variation of the two metallic nanowires in contact with the semiconducting 2D material, Th_1 and Th_2 in Figure 1 (c). Because of set-up limitations, the resistance of each thermometer is measured in a 2-point configuration and we indicate the temperature extracted from this measurement as the "equivalent" temperature, T^{eq}. As explained in Appendix A, the T^{eq} estimation is corrected on the basis of finite elements simulations and control tests in order to extract the effective local

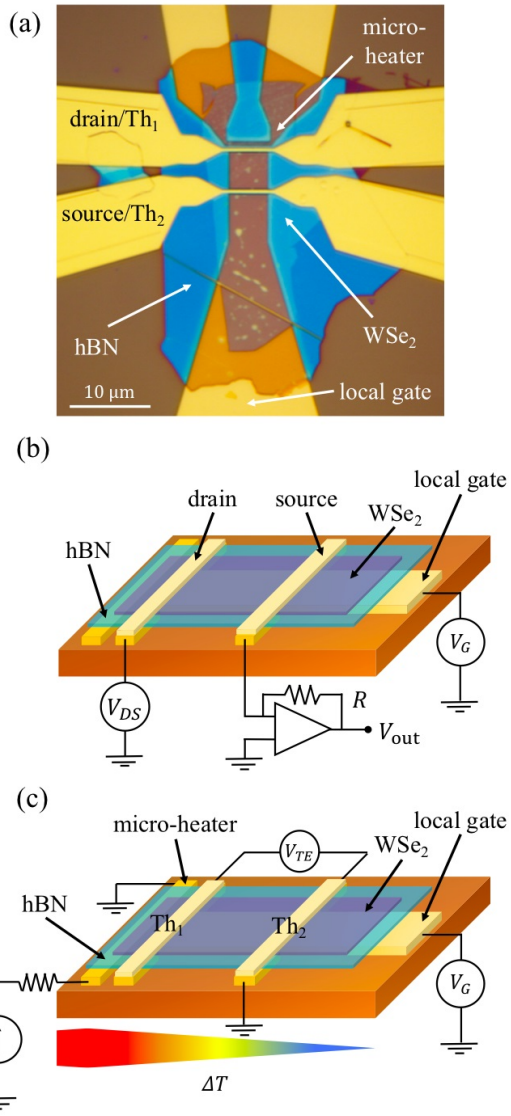

FIG. 1. (a) Optical microscope image of a hBN/WSe_2-based transistor (sample 3). Schematics of the circuitry used for (b) electric and (c) thermoelectric measurements.

temperature rise for each thermometer. The whole ΔT measurement procedure can be divided in two main steps. In the first step, the heater is grounded ($I_{\text{heater}} = 0$) and the temperature of the environment is regulated by the temperature control of the micro probe station molybdenum sample holder in isothermal contact with the sample. A small DC current ($\pm$ 20 μA) is fed by a source-meter (Yokogawa 7651) into the metallic nanowires to measure the induced voltage drop by a nanovoltmeter (Keithley 2182A). The resistance of each line, including the metallic nanowire, is measured as a function of the temperature and it follows the expected linear behavior $R(T) = R_0[1 + \alpha(T - T_0)]$. The temperature coefficient of the resistance α is extracted as $(1/R_0)(dR/dT)$. In the second step, the temperature of the molybdenum plate is fixed at the operating temperature of the experiment, $T_0 = 25$°C. A DC current ramp (from 0 to 5 mA, with steps of 1 mA) is ap-

plied into the micro-heater inducing Joule heating and thus a temperature gradient along the sample. For each value of the heater current I_{heater}, the metallic nanowires resistances, R_1 and R_2, are simultaneously measured. Thanks to the first calibration step, it is possible to evaluate the "equivalent" temperature of Th_1 and Th_2 for a given value of I_{heater}. The curves follow a quadratic trend ($T^{\text{eq}} = aI^2_{\text{heater}} + b$, with $b = T_0$) due to the relation $R \propto T^{\text{eq}} \propto I^2_{\text{heater}}$. The temperature difference between the two thermometers, ΔT^{eq}, is equal to $dT^{\text{eq}}_{\text{Th}_1} - dT^{\text{eq}}_{\text{Th}_2}$, where $dT^{\text{eq}}_{\text{Th}_{1/2}}$ is the temperature increase of each thermometer with respect to T_0. The corrected temperature gradient is evaluated as $\Delta T_{\text{corr}} = \gamma\, dT^{\text{eq}}_{\text{Th}_1} - dT^{\text{eq}}_{\text{Th}_2}$, where γ is a correction factor equal to ~ 2.93 that has been experimentally evaluated and validated by finite element simulations, detailed in Appendix A.

The thermoelectric voltage, V_{TE}, generated by the temperature gradient, is measured as the open-circuit voltage drop between the two electrodes as a function of the applied heating current I_{heater} and gate voltage V_G in the range $\pm$ 25 V. For each value of gate voltage V_G, the current in the heater is swept from 0 to 5 mA (with a current step of 50 μA and a sweeping rate of 50 μA/s) and, for each current value, the open-circuit voltage V_{oc} is measured. The gate voltage is applied by adopting the same electrical connection employed for the electrical measurements, by connecting the thermometer Th_2 to the ground and leaving Th_1 floating. Due to the relationship $V_{\text{TE}} \propto \Delta T \propto I^2_{\text{heater}}$, the recorded $V_{\text{oc}}(I_{\text{heater}})$ exhibits a parabolic behavior as a function of the heating current. To correctly extract the thermoelectric part of the measured signal, we follow the approach proposed by Kayyalha et al.[43]. The measured open-circuit voltage as a function of the heating current is of the form $V_{\text{oc}}(I_{\text{heater}}) = \hat{a} I^2_{\text{heater}} + \hat{b} I_{\text{heater}} + \hat{c}$, meaning that its nature is not purely thermoelectric. The constant term ($\hat{c}$) corresponds to the contribution of the voltmeter offset and the resistive coupling between the semiconducting channel and the gate. The linear term ($\hat{b} I_{\text{heater}}$) indicates the contributions of coupling from the heater to the channel. Finally, the second order term ($\hat{a} I^2_{\text{heater}}$) is the pure thermoelectric contribution, V_{TE}, to the measured signal. Thus, the Seebeck coefficient is obtained for each value of gate voltage V_G as the slope of the V_{TE} vs. ΔT_{corr} dependence. Note that, in evaluating the Seebeck coefficient, only data points for which the second-order contribution in the $V_{\text{oc}}(I_{\text{heater}})$ fitting procedure is strictly higher than the linear and constant contributions at the maximum applied current in the heater (I_{heater} = 5 mA) are considered reliable. Data points not matching this criterion have been removed.

III. RESULTS AD DISCUSSION

We present results for four representative devices made with Ag, Pd, Co and Ti metallic electrodes (sample 1, 2, 3 and 4, respectively). For each metal contact, results have been confirmed at least on a second sample with the same geometry of the electrical contacts and similar flakes thicknesses. In all the explored devices, the WSe_2 channel length (L) and width (W) are both equal to ~ 5 μm. The thickness of the flakes composing the heterostructures have been measured by atomic force microscopy (AFM) (Figure 10 in Appendix C). WSe_2 has a thickness varying from 2.8 $\pm$ 0.4 nm to 3.8 $\pm$ 0.4 nm, corresponding to 4 to 6 layers. For such a variability of the layers number we expect the WSe_2 band gap to be affected by less than 10%[44]. Table I summarizes the relevant parameters of the discussed devices.

TABLE I. Samples discussed in this work with metal used for the contact, hBN and WSe_2 thicknesses, and WSe_2 number of layers as determined by AFM.

	metal	d_{hBN} [nm]	d_{WSe_2} [nm]	# of layers
sample 1	Ag	57 ± 3	3.8 ± 0.4	6
sample 2	Pd	45 ± 1	3.0 ± 0.5	4
sample 3	Co	50 ± 3	2.8 ± 0.4	4
sample 4	Ti	41 ± 2	2.9 ± 0.3	4

Figure 2 shows a typical transfer characteristic for (a) n-type transport behavior (sample 1) and (b) ambipolar transport behavior (sample 2) in linear (red data) and semi-log (blue data) scales, with a source-drain polarization $V_{DS} = 2$ V and a gate polarization $|V_G| \leq 25$ V. Note that the gate voltage has been normalized to the hBN thickness, d_{hBN}, in order to allow for a direct comparison between samples. Ambipolar behavior is observed in Pd-, Co- and Ti-based WSe_2-transistors, while devices with Ag contacts result systematically in n-type transport characteristics. The threshold voltage $V_{th-h/e}$ is extracted by extrapolating the linear part of the transfer characteristic to zero I_{DS} as shown in Figure 2 by the dashed black lines.

The device field-effect mobility μ is evaluated as $(L/W)(dI_{DS}/dV_G)(1/C_{\text{hBN}}V_{DS})$, where dI_{DS}/dV_G is the transconductance, $C_{\text{hBN}} = \varepsilon_0\varepsilon_r/d_{\text{hBN}}$ is the dielectric capacitance per unit area, $\varepsilon_0 = 8.854 \times 10^{-12}$ F/m is the vacuum permittivity. Using a 2-point approach for transport measurement, the evaluation of the electron and hole mobilities is limited by the contribution of the interface barriers, and it has to be considered as a lower bound for the intrinsic material carriers mobility. We find out the highest electron (hole) mobility equal to ~ 0.8, ~ 100 (10), ~ 40 (200) and ~ 20 (125) cm^2/ V s for Ag, Pd, Co and Ti, respectively, in agreement with values reported in literature[41,42,45–47]. The density of charge carriers, n_{3D}, can be evaluated at the highest gate voltage by the relation $n_{3D} = \frac{C_{\text{hBN}}}{e\, d_{\text{WSe}_2}}(V_G - V_{th})$ resulting of the order of 10^{19} cm^{-3} for both electrons and holes[17]. All devices have large ON/OFF ratios ($\sim 10^5$) and they all show high subthreshold swings (SS) for both bands injections with typical values in the interval 2000 mV/dec $< SS <$ 5000 mV/dec. The reduced performance of the devices (large SS and low $\mu_{e/h}$) can be caused by intrinsic material impurities and defects related to the fabrication process[30,46]. However, orbital hybridization at the metal/WSe_2 interface plays also a major role by modifying the local DOS in the 2D semiconductor and affecting electric properties. Band structure calculations in WSe_2-based transistors have shown that in the weak hybridization case, a Schottky barrier is created at the metal/semiconductor interface, while strong coupling results in a decay of the metallic wave-

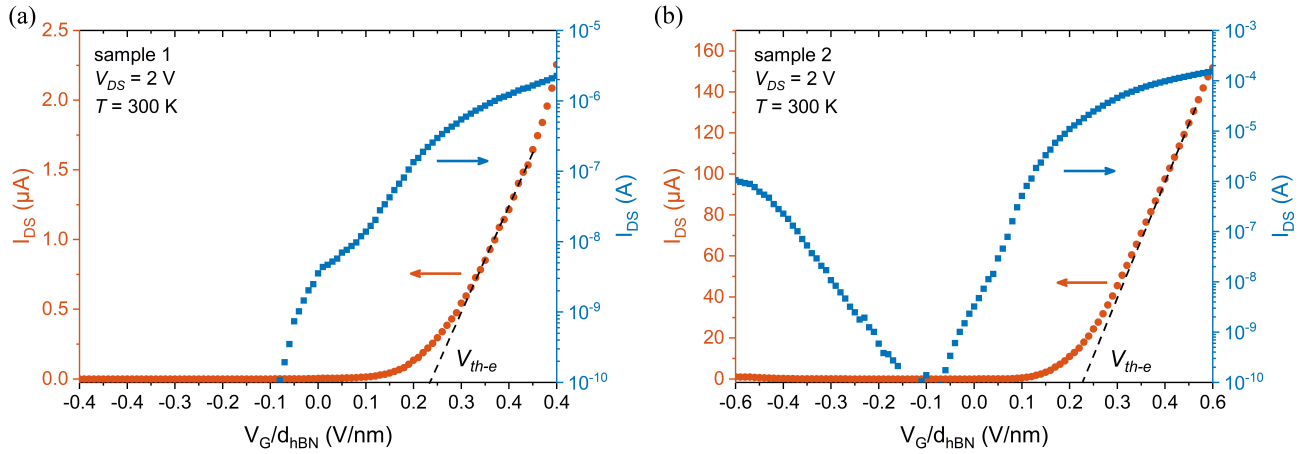

FIG. 2. Transfer characteristic of (a) sample 1 (Ag contacts) and (b) sample 2 (Pd contacts) in linear (red) and logarithmic (blue) scale at $T = 300$ K and $V_{DS} = 2$ V. The gate voltage on the x-axis has been normalized to d_{hBN}. Black dashed lines indicate the extrapolation of the linear part of the transfer characteristics to extract the threshold voltage at zero I_{DS}.

function into the nanometer thin 2D semiconductor. In this case, the Schottky barrier is generated between the hybridized 2D material and the 2D channel[34,35,48]. Moreover, electronic states appear in the original band gap of WSe_2, playing a fundamental role in Fermi level pinning and charge injection[49]. Wang et al. have theoretically demonstrated that Al, Ag and Au, result in weak metal/WSe_2 bonding with a preserved band gap, while Pd and Pt, induce a stronger metal/WSe_2 bonding with a highly reduced band gap and ambipolar expected transfer characteristics[34]. As bonding strength can be understood in terms of d-band hybridization, we expect strong coupling for Co and Ti contacts, having these metals partially filled d-shells. Band structure calculations in the case of Ti/$MoSe_2$ confirm this expectation[35]. The ambipolar behavior observed with Pd, Co and Ti is coherent with calculations of Schulman et al. where pinning for Pd and Ni is predicted almost in the middle of the gap[50]. Results with Ag contacts (sample 1) are consistent with these observations. In the case of Ag-based transistors, the device is always in the OFF-state for hole injection, while it switches to the ON-state for electron injection.

We have evaluated the Schottky barrier heights using the back-to-back Schottky diode (BBSD) model[51]. According to this model, the source and drain contacts on the 2D material can be represented as two diodes connected in a back-to-back configuration. Depending on the source-drain bias voltage V_{DS}, the overall current will be limited by the reverse biased diode. The Schottky barriers can be extracted by fitting the device output characteristics to the thermionic transport equation of a reversed diode. Figure 3 shows two representative output characteristics (sample 3) for $V_G = 6.5$ V (black data) and $V_G = -6.5$ V (red data), corresponding to the subthreshold electron and hole injection regimes, respectively. The solid lines are the corresponding fits to the BBSD model. The inset shows the extracted values of the barrier, ϕ_B, as a function of gate voltage in the range $|V_G| \leq 25$ V. The actual electron (hole) Schottky barrier height, $\phi_{SBe(h)}$, is defined at the flat band condition, identified as the gate voltage for which the barrier height diverges from the linear trend, as indicated by the solid red lines. We find out similar values of ϕ_{SBe} and ϕ_{SBh} of about 0.2 - 0.3 eV for Pd, Co and Ti, in agreement with previous works[52–54]. The sum of the electron and hole barriers defines a reduced energy gap of the order of 0.5 - 0.6 eV, well below the predicted value for 4 - 6 layers WSe_2 of 1.1 - 1.2 eV[44,55]. Such a strong reduction can be attributed to the presence of gap states in the WSe_2 band gap due to material impurities as well as strong hybridization at the metal/2D material interface[34]. In the case of Ag contacts (sample 1), only the electron barriers can be extracted which result of the order of 0.46 eV, higher than the values estimated for the other samples. The expected band gap is thus > 0.46 eV, higher than the previous estimation. This result is in agreement with the predicted weak coupling nature of the Ag/WSe_2 interface.

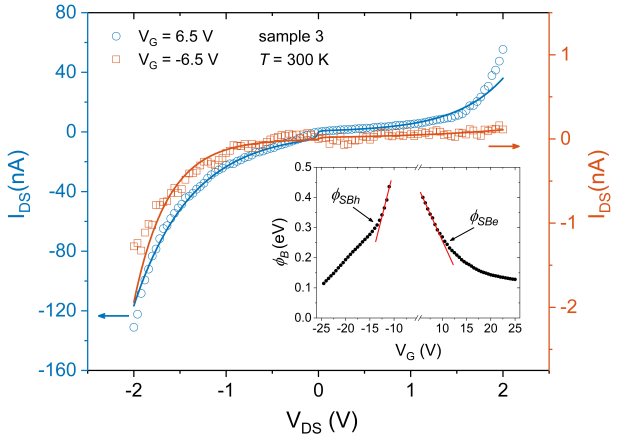

FIG. 3. Output characteristics of sample 3 (Co contacts) at $V_G = 6.5$ V (black data, left axis) and $V_G = -6.5$ V (red data, right axis). Solid lines are fits to the BBSD model. Inset: Schottky barriers extraction at flat band condition.

We move now our attention to the thermoelectric characterization of the presented devices focusing on the Seebeck co-

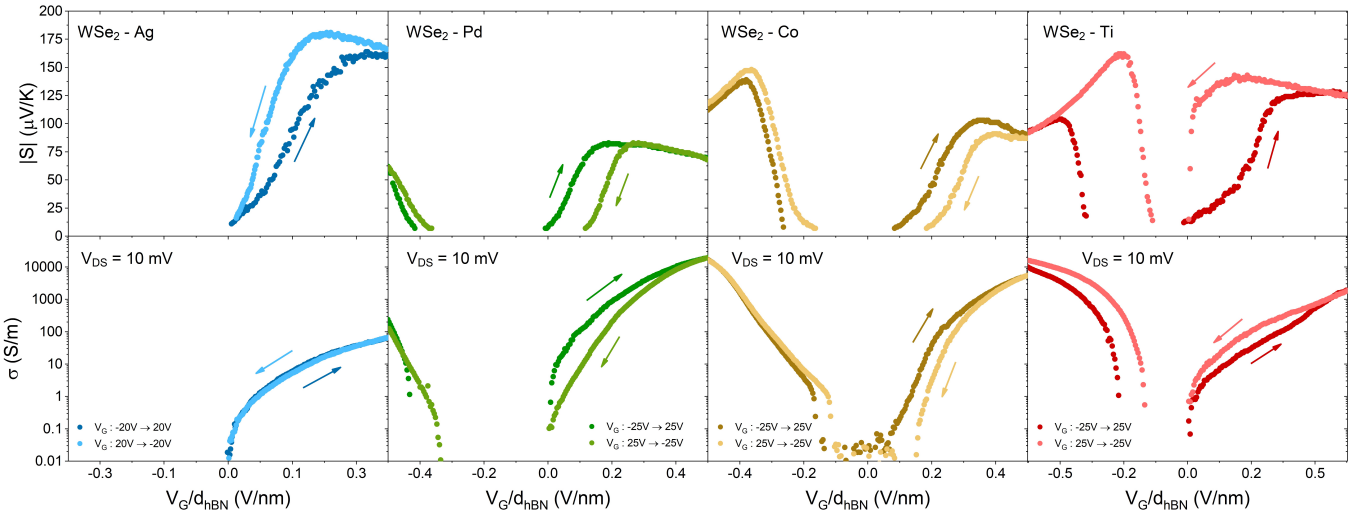

FIG. 4. Absolute value of the Seebeck coefficient (top panel) and electrical conductivity measured at $V_{DS} = 10$ mV (bottom panel) for the four discussed samples, for increasing and decreasing gate voltage sweeps (as indicated by the arrows). The gate voltage on the x-axis has been normalized to d_{hBN}.

efficient. Figure 4 (upper panel) shows the absolute value of the Seebeck coefficient as a function of the gate voltage normalized to d_{hBN}, for increasing and decreasing gate voltage sweep (as indicated by the arrows). The sign of S reveals the nature of the majority carriers, negative for $V_G > 0$ (electron injection) and positive for $V_G < 0$ (hole injection). No signal can be revealed in the gap region, where the density of charge carriers goes to zero. Moreover, in this region the signal is measured with higher uncertainty since the device impedance becomes very high. The measured S increases suddenly as the Fermi level moves towards the conduction or the valence band edges. When further increasing the density of charge carriers, S decreases as expected, being roughly $\propto 1/n_{3D}$ (beyond threshold). In all cases, the measured values of the Seebeck coefficient are in agreement with what previously reported in literature for WSe_2-based transistors[17,18]. The maximum S values, $|S_{max}|$, are of the order of 180 ± 11 μV/K for Ag, 80 ± 2 μV/K for Pd, 150 ± 2 μV/K for Co and 160 ± 4 μV/K for Ti. The thermoelectric measurements confirm the ambipolar behavior in Pd-, Co- and Ti-contacted devices. The preferred electron injection for Ag-based transistors is also in agreement with the observations done on the electrical characterization. Figure 4 (bottom panel) shows the devices conductivity as function of the reduced gate voltage (trans-conductance curves) measured in this case at low source-drain polarization ($V_{DS} = 10$ mV) for the four samples in the two gate sweep directions (as indicated by the arrows). For the sake of clarity, we summarize on Table II the relevant electric and thermoelectric parameters extracted for each samples, namely the electron and hole barrier heights, the maximum Seebeck coefficient and the maximum electrical conductivity and the electron and hole mobilities.

By comparing the four samples presented in Figure 4, it appears that the nature of the metallic contact has an impact on both the electric and thermoelectric response of the studied WSe_2-based devices. The thermoelectric power and the low bias electrical conductivity vary rather gently close to the conduction and valence bands edges, with finite slopes that depend on the measurement sweep direction. The slopes of S and σ at the band edges are typically related to the presence of gap states close to the valence band maximum or the conduction band minimum, inducing an exponential tail of the DOS in the band gap region. A metal dependent reduction of the band gap is also suggested by the different extension of the OFF-state in the electric and thermoelectric measurements, directly compared on Figure 4 by normalizing the gate voltage to d_{hBN}. The S coefficient is different from zero for positive and negative gate voltage for Pd-, Co- and Ti- based devices, in agreement with the observed ambipolar transport, while a finite S coefficient is only measured for Ag-based devices for positive gate voltages and no signal is detected at negative gate voltages. All S and σ measurements show a hysteretic behavior, particularly evident in sample 4. This phenomenon is recurrent in TMDs field effect transistors and is often related to the gate voltage stress[26,56,57].

It is worthwhile to note that a trend can be recognized in the electron-doped region in the electric and thermoelectric

TABLE II. Electron and hole barrier heights, maximum Seebeck coefficient, maximum electrical conductivity, electron and hole mobilities for each sample discussed in this work.

	ϕ_e [eV]	ϕ_h [eV]	$\lvert S_{max} \rvert$ [μV/K]	σ_{max} [S/m]	μ_e [cm^2/Vs]	μ_h [cm^2/Vs]
sample 1	0.46	–	181[a]	67[a]	0.8	–
sample 2	0.2	0.27	83[a]	21.5×10^3 [a]	100	10
sample 3	0.2	0.11	148[b]	17×10^3 [b]	40	200
sample 4	0.22	0.23	162[b]	16×10^3 [b]	20	125

[a] electron doping
[b] hole doping

properties when looking at the samples in the order 2-3-4-1 (Pd-Co-Ti-Ag contacts): the mobility and the electrical conductivity decrease while the barrier height and Seebeck coefficient increase. No similar trend is observed in the hole-doped regime. The empirical trend in the electron-doped region is coherent with the predicted weak and strong hybridization theoretically calculated for Ag/WSe_2 and Pd/WSe_2 interface, respectively. Weak interface coupling at the Ag/WSe_2 interfaces allows to consider the thermoelectric response as mostly related to the WSe_2 electronic structure in the channel rather than under the contacts. In this case, we measure the highest Seebeck coefficient. Strong coupling, expected at the Pd/WSe_2, improves charge injection and mobility, while reducing the thermoelectric response. No theoretical predictions exist for the other metal contacts used. In these cases, since the bonding strength is related to *d*-band hybridization and having these metals partially filled *d*-shells, we can also expect strong coupling at the interface. We also note that the measured low-voltage 2-point electrical conductivity is lower in the case of Ag-based devices ($\sigma_{max} \sim 10^2$ S/m) with respect to Pd-, Co- and Ti-based devices ($\sigma_{max} \sim 10^4$ S/m) by a factor of 10^2, while the Seebeck coefficient has the highest value in the case of Ag-based devices and it is only reduced by a factor of 1.1 - 2 in the case of the devices with the other metal contacts. This general trend is confirmed also in the other measured devices (not shown in this work). Note that in actual devices, contact resistance at the interface can affect the measurement of the Seebeck effect. However, we exclude that our measurements are contact dominated, since a reduced Seebeck coefficient would be expected for devices exhibiting the lower 2-point electrical conductivity, which is contrary to what we observe experimentally.

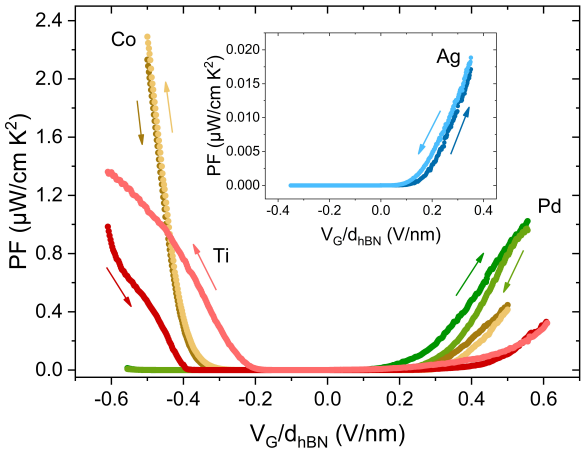

FIG. 5. Power factor estimated for the four discussed samples as a function of the gate voltage for the two sweep directions as indicated by the arrows. The gate voltage on the x-axis has been normalized to d_{hBN}. The inset shows a zoom for the case of Ag-based device (sample 1).

The power factor, $PF = S^2\sigma$, is estimated for the four samples, as illustrated in Figure 5, as a function of the normalized gate voltage. In the inset of Figure 5 it is reported a zoom for the Ag-based device (sample 1) which shows the lowest values of *PF*. The highest *PF* are observed for Pd-, Co- and Ti-based devices with maximum values, PF_{max}, ranging between 1.4 and 2.4 μW/cm K^2 with an error of 0.4 μW/cm K^2. Such values are comparable with what reported in literature for WSe_2[18,19]. It is worthy to notice that Yoshida et al.[17] find higher values of *PF* by adopting a 4-point approach to measure the electrical conductivity of few-layers WSe_2 on SiO_2 substrate. In our case, due to our set-up limitation, *PF* is under-estimated since σ is obtained by a 2-point measurement technique. Thus, a remarkable enhancement of the power factor is expected in our devices if a 4-probe conductivity measurement would be performed at least in the conducting gate voltage region. By considering a value of WSe_2 in-plane thermal conductivity $\kappa = 1.4$ W/mK as extracted from the literature[20,23], we evaluate room temperature figures of merit, $ZT_{300\mathrm{K}}$, on the order of $2 \times 10^{-4} \pm 0.6 \times 10^{-4}$ for Ag-based samples and in the range 0.02 - 0.08 for Pd-, Co- and Ti-WSe_2 samples with an error of 0.01, revealing the potential of contact engineering on TMDs for TE applications.

IV. CONCLUSIONS

In conclusion, we have experimentally investigated the effect of different metal contacts (Ag, Pd, Co and Ti) on the electric and thermoelectric properties of hBN-supported few layers WSe_2 transistors. We have simultaneously measured the gate voltage dependence of σ and *S* and pointed out thermoelectric power values consistent with the literature, with S_{max} as large as 180 μV/K. Our results are qualitatively coherent with the theoretically predicted electronic properties of WSe_2-based devices when orbital hybridization at the metal-semiconductor interface are taken into account. In contrast with the S-σ anti-correlation, strong hybridization enhances the device electrical conductivity by a factor of 10^2 with respect to the weak hybridization case, still preserving comparable values of the Seebeck coefficient, potentially allowing for an increased power factor, *PF*. Orbital hybridization effects are also consistent with the reduced semiconducting band gap revealed from both the electric and thermoelectric investigation. Several theoretical works have investigated the effect of different metal/2D material interface on the local density of state, including the case of WSe_2. However, to our knowledge, no experimental study exists in literature exploring such interface effect simultaneously on the electric and thermoelectric properties of 2D materials. Our results unveil contact engineering as a useful tool to improve the thermoelectric performances of actual WSe_2-based devices. Promoting strong interface coupling allows improving the power factor of TMDs-based devices for an optimized thermoelectric response.

ACKNOWLEDGMENTS

This research was funded by The Commissariat Général à l'Investissement d'Avenir and the Agence Nationale de la Recherche (grant number ANR-20-CE05-0045-01). The au-

thors thank P. Filloux and R. Duhamel for technical support in the clean room of the Laboratoire Matériaux et Phénomènes Quantiques (UMR 7162) at the Université de Paris. For the purpose of open access, the authors have applied a CC-BY public copyright licence to any Author Accepted Manuscript (AAM) version arising from this submission.

DATA AVAILABILITY STATEMENT

The data that support the findings of this study are available from the corresponding author upon request.

Appendix A: Temperature gradient measurement

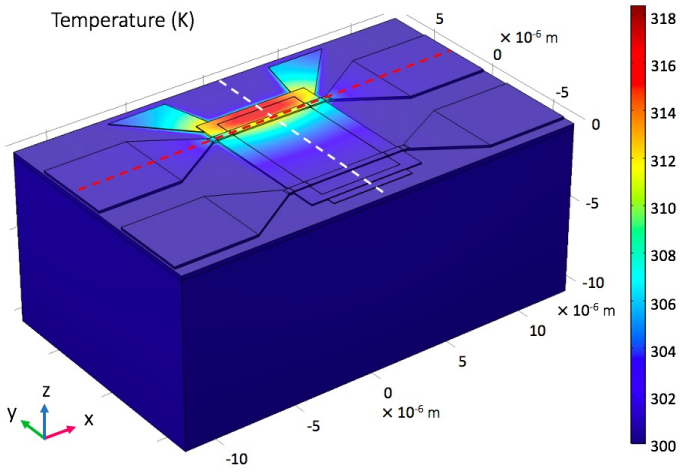

FIG. 6. Device geometry simulated using COMSOL multiphysics. The color legend indicates the temperature at the outermost surface of the device.

The Seebeck coefficient is defined by the ratio between the open-circuit thermoelectric voltage V_{TE} and the temperature gradient ΔT inducing it, $S = -V_{\mathrm{TE}}/\Delta T$. In a standard DC approach[17,29,43,58], the local temperature rise due to Joule-heating in the micro-heater is measured by the resistance variation of two local thermometers, Th_1 and Th_2. The reduced number of contacts (8) in our probe-station does not allow us to simultaneously connect all the device parts (Th_1, Th_2, gate and micro-heater) to perform a 4-point measurement of the thermometers resistances simultaneously. This would be only possible by breaking the vacuum in the micro probe station chamber. Since the interaction with the atmosphere could modify the 2D material properties, we decided to adopt the "equivalent" 2-point approach described in the main text to measure the thermometers resistance and successively correct the extracted T^{eq} on the basis of finite element simulations and experimental tests explained in the following.

Finite element modeling (FEM) using COMSOL multiphysics is employed to simulate the temperature gradients developed in the device, as shown Figure 6. In the simulated device, the thickness of the hBN and WSe_2 layers are equal to 40 nm and 3 nm, respectively. All relevant physical parameters, such as the electrical conductivity σ, the thermal conductivity κ, the mass density ρ, the electrical permittivity ε have been extracted from the literature[20,23,59]. The electrical conductivity of the WSe_2 is extracted from our experimental data in the ON-state.

Joule heating is achieved by injecting an electric current (I_{heater} in the range from 1 to 5 mA) at one extremity of the micro-heater while grounding the other extremity, as done experimentally. Figure 7 shows the temperature profiles on the WSe_2 surface: (a) in the device longitudinal y-direction, following the white dashed line in Figure 6 and (b) along thermometer Th_1 in the x-direction, following the red dashed line in Figure 6. The simulated longitudinal profiles (Figure 7 (a)) confirm that only the thermometer closer to the heater (Th_1) is subjected to a significant temperature increase while the second thermometer (Th_2) does not show a significant temperature rise and it is almost thermalized at the temperature of the environment. The profiles extracted along the x-direction of the thermometer Th_1 (Figure 7 (b)) show that the main temperature increase occurs over the sample region ($|x| < 2.5$ μm). For each I_{heater}, we have evaluated the average temperature T^* of Th_1 by integrating the temperature profile in Figure 7 (b) in the region $|x| < 3$ μm, which corresponds to the temperature that would be extracted from a standard 4-point resistance calibration. We have also evaluated the average temperature, T^{eq}, of the whole metallic line by integrating the temperature profile in the region $|x| < 25$ μm, corresponding to the whole length of the metallic line. This corresponds to the "equivalent" 2-point approach experimentally used. The obtained temperature are plotted in the inset of Figure 7 (b) as a function of I^2_{heater}. The ratio of the temperature increases dT^*/dT^{eq}, turns out to be a constant equal to 2.76, independently of the current injected in the micro-heater.

Control measurements have been carried out on three devices equivalent to the ones presented in the main text, with the same electrodes geometry and similar hBN and WSe_2 flakes dimensions and thicknesses, to confirm the simulated results. These test samples are designed with 4-probes thermometers. For each thermometer, we have separately evaluated the temperature coefficient of resistance in a 4-point and 2-point configuration as a function of the temperature of the environment. Successively, we have measured the temperature of each thermometer as a function of the applied current in the micro-heater on the basis of the two calibration configurations. Figure 8 illustrates a representative example of such a temperature measurements (T^* and T^{eq}) for the two thermometers, Th_1 (Figure 8 (a)) and Th_2 (Figure 8 (b)), on the basis of the 4-point and 2-point calibration configuration, respectively. Dashed lines are the linear fits to the data ($T = aI^2_{\mathrm{heater}} + b$). These test measurements require the opening of the vacuum chamber to change the electrical connections from one thermometer to the other, which exposes the 2D material to atmosphere, adsorption of gas or water molecules, not beneficial to preserve its properties. As expected, Figure 8 shows that the temperature increase in Th_1 is larger when measured in the 4-point configuration. From this test measurements we extract a ratio dT^*/dT^{eq} equal to

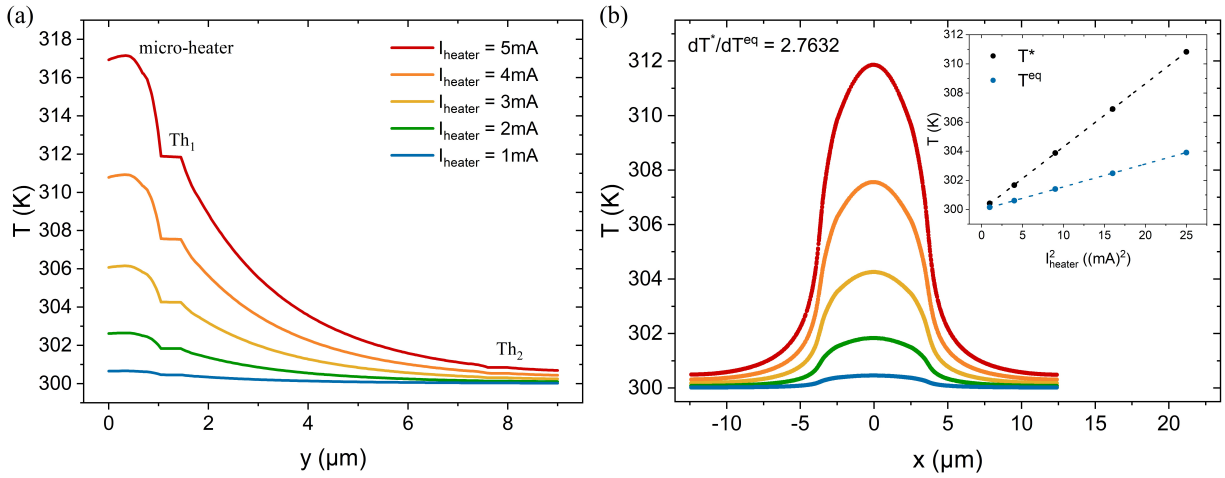

FIG. 7. (a) Temperature profile in the longitudinal direction of the device at $x = 0$ and z corresponding to the WSe_2 surface when the current in the micro-heater is varied from 1 mA (blue line) to 5 mA (red line). (b) Temperature profile developed in the thermometer Th_1 as a function of injected current in the micro-heater. The inset shows the simulated T^* and T^{eq} as a function of I^2_{heater}. Dashed lines are the linear fit to the data.

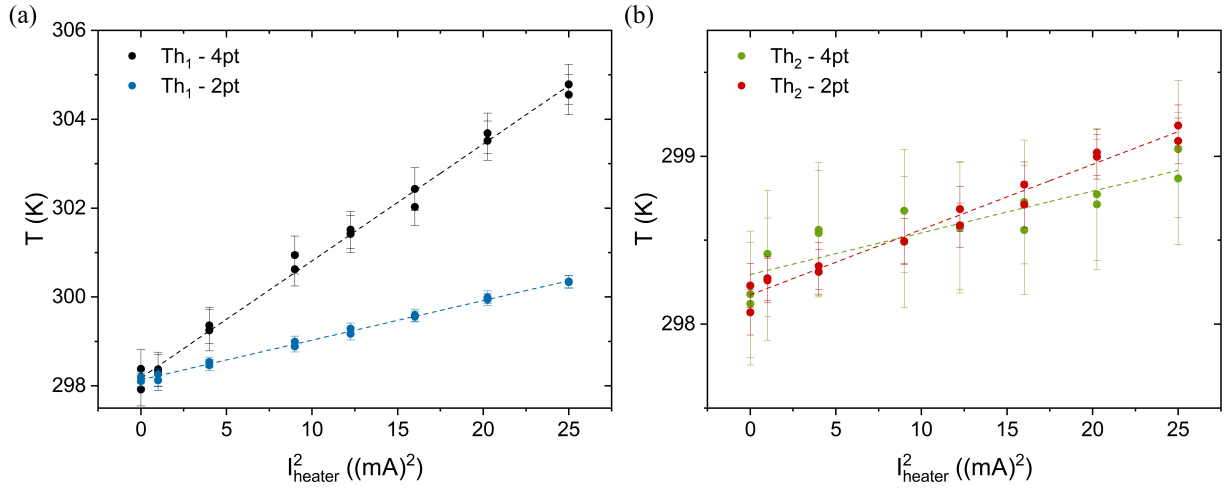

FIG. 8. (a) Local temperature increase measured by the thermometers Th_1 with the 4-point and 2-point configuration (black and blue dots, respectively) when Joule heating occurs in the micro-heater. (b) Local temperature increase measured by the thermometers Th_2 with the 4-point and 2-point configuration (green and red dots, respectively) when Joule heating occurs in the micro-heater. Dashed lines represent the linear fit to the data.

2.947 ± 0.007. The temperature increase in Th_2, instead, is lower than 1 K, in both measurement configuration (red and green data in Figure 8 (b)). This confirms that Th_2 is nearly in thermal equilibrium with the environment. For the three samples, we have found the same results with a constant dT^*/dT^{eq} ratio for Th_1, equal to $\gamma = 2.93 \pm 0.06$. This analysis is in agreement with the COMSOL simulation (Figure 7 (a)). The γ value extracted experimentally is used in the main text as correction factor for the estimation of the temperature increase of thermometer Th_1. By considering the estimated error bars of ~ 0.5 K in Figure 7 (b), we have chosen to assume $dT^*/dT^{eq} \sim 1$ for Th_2.

Supported by the FEM simulations and the experimental tests, we have empirically corrected the measured 2-point "equivalent" temperature gradient $\Delta T^{eq} = dT^{eq}_{Th_1} - dT^{eq}_{Th_2}$ in the longitudinal direction of the sample by the experimentally evaluated γ factor as follow:

$$\Delta T_{corr} = \gamma\, dT^{eq}_{Th_1} - dT^{eq}_{Th_2} \tag{A1}$$

which is the relation introduced in the main text, on Section II.

Appendix B: Measurement of the thermoelectric voltage

We show here an example of the measured open-circuit voltage V_{oc} as a function of the heating current, I_{heater}, in the case of sample 3 at two different gate voltages, $V_G = 25$ V and

V_G = -10 V. As explained in the main text, V_{oc} has not a purely quadratic trend but, depending on the gate voltage, a linear and a constant term appear related to the coupling between the heater and the channel and to the contribution of the voltmeter offset and the resistive coupling between the semiconducting channel and the gate. Figure 9 (a) shows data at V_G = 25 V, corresponding to the ON-state of sample 3. The experimental data (blue points) are well described by a quadratic fit (red continuous line), demonstrating that in this gate voltage range the quadratic behavior dominates the linear and constant spurious terms. Figure 9 (b) shows data at V_G = -10 V, nearly in the OFF-state of sample 3. In this case, the extra spurious terms start to play a role. The thermometric contribution V_{TE} is always extracted as the purely quadratic part of V_{oc} as a function of I_{heater}.

Appendix C: AFM characterization

Atomic force microscopy (AFM) is used to determine the thicknesses of the hBN and WSe_2 layers for the discussed samples. Figure 10 shows AFM images for (a) sample 1 (Ag contacts), (b) sample 2 (Pd contacts), (c) sample 3 (Co contacts) and (d) sample 4 (Ti contacts). In all cases, we show a large area ($\sim 50\times50\ \mu m^2$) image of the whole device and a zoom on a smaller area of few μm^2 (red rectangles) where an example of line profile of the WSe_2 step is reported. The hBN and WSe_2 thicknesses are listed in Table I of the main text and have been evaluated by averaging 50 step heights of line profiles taken in different samples zones.

[1] L. E. Bell, "Cooling, heating, generating power, and recovering waste heat with thermoelectric systems," Science **321**, 1457–1461 (2008).

[2] J. R. Sootsman, D. Y. Chung, and M. G. Kanatzidis, "New and old concepts in thermoelectric materials," Angew. Chem. Int. Ed. **48**, 8616–8639 (2009).

[3] J. J. Urban, A. K. Menon, Z. Tian, A. Jain, and K. Hippalgaonkar, "New horizons in thermoelectric materials: Correlated electrons, organic transport, machine learning, and more," J. Appl. Phys. **125**, 180902 (2019).

[4] V. Leonov and R. J. M. Vullers, "Wearable thermoelectric generators for body-powered devices," J. Electron. Mater. **38**, 1491–1498 (2009).

[5] F. Suarez, D. P. Parekh, C. Ladd, D. Vashaee, M. D. Dickey, and M. C. Öztürk, "Flexible thermoelectric generator using bulk legs and liquid metal interconnects for wearable electronics," Appl. Energy **202**, 736–745 (2017).

[6] L. L. Baranowski, G. J. Snyder, and E. S. Toberer, "Concentrated solar thermoelectric generators," Energy Environ. Sci. **5**, 9055–9067 (2012).

[7] N. R. Kristiansen, G. J. Snyder, H. K. Nielsen, and L. Rosendahl, "Waste heat recovery from a marine waste incineratorusing a thermoelectric generator," J. Electron. Mater. **41**, 1024–1029 (2012).

[8] L. D. Hicks and M. S. Dresselhaus, "Effect of quantum-well structures on the thermoelectric figure of merit," Phys. Rev. B **47**, 12727–12731 (1993).

[9] L. D. Hicks and M. S. Dresselhaus, "Thermoelectric figure of merit of a one-dimensional conductor," Phys. Rev. B **47**, 16631–16634 (1993).

[10] M. S. Dresselhaus, G. Chen, M. Y. Tang, R. G. Yang, H. Lee, D. Z. Wang, Z. F. Ren, J.-P. Fleurial, and P. Gogna, "New directions for low-dimensional thermoelectric materials," Adv. Mater. **19**, 1043–1053 (2007).

[11] J. He and T. M. Tritt, "Advances in thermoelectric materials research: Looking back and moving forward," Science **357**, eaak9997 (2017).

[12] Q. H. Wang, K. Kalantar-Zadeh, A. Kis, J. N. Coleman, and M. S. Strano, "Electronics and optoelectronics of two-dimensional transition metal dichalcogenides," Nature Nanotechnol. **7**, 699–712 (2012).

[13] K. F. Mak and J. Shan, "Photonics and optoelectronics of 2D semiconductor transition metal dichalcogenides," Nat. Photonics **10**, 216–226 (2016).

[14] M. Buscema, M. Barkelid, V. Zwiller, H. S. J. van der Zant, G. A. Steele, and A. Castellanos-Gomez, "Large and tunable photothermoelectric effect in single-layer MoS_2," Nano Lett. **13**, 358–363 (2013).

[15] J. Wu, H. Schmidt, K. K. Amara, X. Xu, G. Eda, and B. Özyilmaz, "Large thermoelectricity via variable range hopping in chemical vapor deposition grown single-layer MoS_2," Nano Lett. **14**, 2730–2734 (2014).

[16] M.-S. Kang, S.-Y. Kang, W.-Y. Lee, N.-W. Park, K. C. Kown, S. Choi, G.-S. Kim, J. Nam, K. S. Kim, E. Saitoh, H. W. Jang, and S.-K. Lee, "Large-scale MoS_2 thin films with a chemically formed holey structure for enhanced seebeck thermopower and their anisotropic properties," J. Mater. Chem. A **8**, 8669–8677 (2020).

[17] M. Yoshida, T. Iizuka, Y. Saito, M. Onga, R. Suzuki, Y. Zhang, Y. Iwasa, and S. Shimizu, "Gate-optimized thermoelectric power factor in ultrathin WSe_2 single crystals," Nano Lett. **16**, 2061–2065 (2016).

[18] J. Pu, K. Kanahashi, N. T. Cuong, C.-H. Chen, L.-J. Li, S. Okada, H. Ohta, and T. Takenobu, "Enhanced thermoelectric power in two-dimensional transition metal dichalcogenide monolayers," Phys. Rev. B **94**, 014312 (2016).

[19] W. Kim, H. Kim, T. Hallam, N. McEvoy, R. Gatensby, H. C. Nerl, K. O'Neill, R. Siris, G.-T. Kim, and G. S. Duesberg, "Field-dependent electrical and thermal transport in polycrystalline WSe_2," Adv. Mater. Interfaces **5**, 1701161 (2018).

[20] C. Chiritescu, D. G. Cahill, N. Nguyen, D. Johnson, A. Bodapati, P. Keblinski, and P. Zschack, "Ultralow thermal conductivity in disordered, layered WSe_2 crystals," Science **315**, 351–353 (2007).

[21] A. Mavrokefalos, N. T. Nguyen, M. T. Pettes, D. C. Johnson, and L. Shi, "In-plane thermal conductivity of disordered layered WSe_2 and $(W)_x(WSe_2)_y$ superlattice films," Appl. Phys. Lett. **91**, 171912 (2007).

[22] W.-X. Zhou and K.-Q. Chen, "First-principles determination of ultralow thermal conductivity of monolayer WSe_2," Sci. Rep. **5**, 15070 (2015).

[23] P. Norouzzadeh and D. J. Singh, "Thermal conductivity of single-layer WSe_2 by a stillinger–weber potential," Nanotechnology **28**, 075708 (2017).

[24] M. Ishigami, J. H. Chen, W. G. Cullen, M. S. Fuhrer, and E. D. Williams, "Atomic structure of graphene on SiO_2," Nano Lett. **7**, 1643–1648 (2007).

[25] J. Martin, N. Akerman, G. Ulbricht, T. Lohmann, J. H. Smet, K. von Klitzing, and A. Yacoby, "Observation of electron–hole puddles in graphene using a scanning single-electron transistor," Nat. Phys. **4**, 144–148 (2008).

[26] C. Lee, S. Rathi, M. A. Khan, D. Lim, Y. Kim, S. J. Yun, D.-H. Youn, K. Watanabe, T. Taniguchi, and G.-H. Kim, "Comparison of trapped charges and hysteresis behavior in hBN encapsulated single MoS_2 flake based field effect transistors on SiO_2 and hBN substrates," Nanotechnology **29**, 335202 (2018).

[27] C. R. Dean, A. F. Young, I. Meric, C. Lee, L. Wang, S. Sorgenfrei, K. Watanabe, T. Taniguchi, P. Kim, K. L. Shepard, and J. Hone, "Boron nitride substrates for high-quality graphene electronics," Nature Nanotech. **5**, 722–726 (2010).

[28] J. Duan, X. Wang, X. Lai, G. Li, K. Watanabe, T. Taniguchi, M. Zebarjadi, and E. Y. Andrei, "High thermoelectricpower factor in graphene/hBN devices," Proc. Natl. Acad. Sci. USA PNAS **113**, 14272–14276 (2016).

[29] J. Wu, Y. Liu, Y. Liu, Y. Cai, Y. Zhao, H. K. Ng, K. Watanabe, T. Taniguchi, G. Zhang, C.-W. Qiu, D. Chi, A. H. C. Neto, J. T. L. Thong, K. P. Loh, and K. Hippalgaonkar, "Large enhancement of thermoelectric performance in MoS_2/h-BN heterostructure due to vacancy-induced band hybridization," Proc. Natl. Acad. Sci. U.S.A. **117**, 13929–13936 (2020).

[30] W. Liu, J. Kang, D. Sarkar, Y. Khatami, D. Jena, and K. Banerjee, "Role of metal contacts in designing high-performance monolayer n-type WSe_2 field effect transistors," Nano Lett. **13**, 1983–1990 (2013).

[31] C.-H. Chen, C.-L. Wu, J. Pu, M.-H. Chiu, P. Kumar, T. Takenobu, and L.-J. Li, "Hole mobility enhancement and p-doping in monolayer WSe_2 by gold decoration," 2D Materials **1**, 034001 (2014).

[32] S. Das and J. Appenzeller, "WSe_2 field effect transistors with enhanced ambipolar characteristics," Appl. Phys. Lett. **103**, 103501 (2013).

[33] H.-J. Chuang, X. Tan, N. J. Ghimire, M. M. Perera, B. Chamlagain, M. M.-C. Cheng, J. Yan, D. Mandrus, D. Tománek, and Z. Zhou, "High mobility WSe_2 p- and n-type field-effect transistors contacted by highly doped graphene for low-resistance contacts," Nano Lett. **14**, 3594–3601 (2014).

[34] Y. Wang, R. X. Yang, R. Quhe, H. Zhong, L. Cong, M. Ye, Z. Ni, Z. Song, J. Yang, J. Shi, J. Li, and J. Lu, "Does p-type ohmic contact exist in WSe_2–metal interfaces?" Nanoscale **8**, 1179–1191 (2016).

[35] Y. Pan, S. Li, M. Ye, R. Quhe, Z. Song, Y. Wang, J. Zheng, F. Pan, W. Guo, J. Yang, and J. Lu, "Interfacial properties of monolayer $MoSe_2$–metal con-

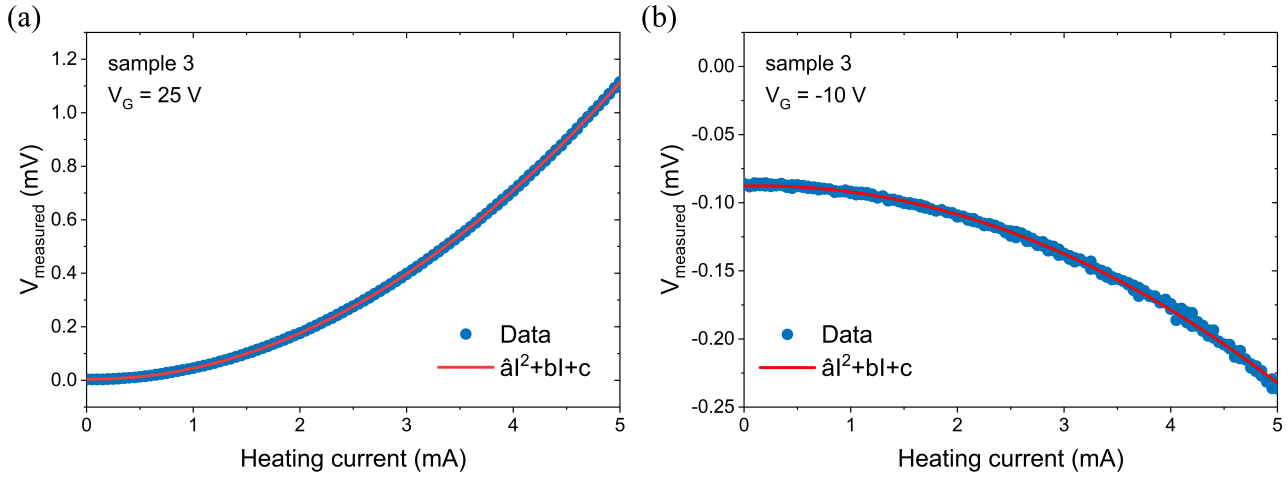

FIG. 9. Open-circuit voltage V_{oc} measured as a function of the heating current I_{heater} for sample 3 at (a) V_G = 25 V and (b) V_G = -10 V.

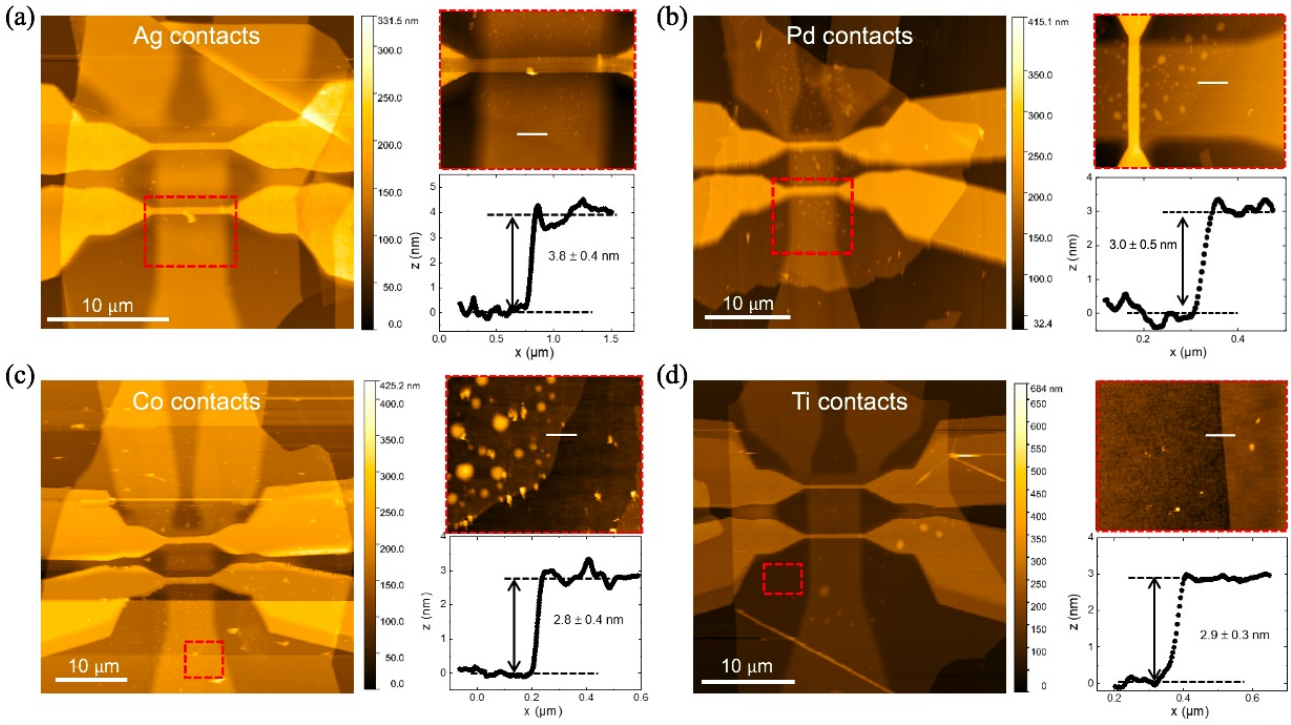

FIG. 10. AFM images for (a) sample 1 with Ag contacts, (b) sample 2 with Pd contacts, (c) sample 3 with Co contacts and (d) sample 4 with Ti contacts. In each case, a zoom (red rectangles) with an example of line profile indicating the WSe_2 thickness is reported.

tacts," J. Phys. Chem. C **120**, 13063–13070 (2016).
[36]D. Çakır and F. M. Peeters, "Dependence of the electronic and transport properties of metal-$MoSe_2$ interfaces on contact structures," Phys. Rev. B **89**, 245403 (2014).
[37]F. Pizzocchero, L. Gammelgaard, B. S. Jessen, J. M. Caridad, L. Wang, J. Hone, P. Bøggild, and T. J. Booth, "The hot pick-up technique for batch assembly of van der Waals heterostructures," Nat. Commun. **7**, 11894 (2016).
[38]K. Hippalgaonkar, Y. Wang, Y. Ye, D. Y. Qiu, H. Zhu, Y. Wang, J. Moore, S. G. Louie, and X. Zhang, "High thermoelectric power factor in two-dimensional crystals of MoS_2," Phys. Rev. B **95**, 115407 (2017).
[39]Z. Wang, Q. Li, Y. Chen, B. Cui, Y. Li, F. Besenbacher, and M. Dong, "The ambipolar transport behavior of WSe_2 transistors and its analogue circuits," NPG Asia Mater. **10**, 703–712 (2018).
[40]W.-M. Kang, S. Lee, I.-T. Cho, T. H. Park, H. Shin, C. S. Hwang, C. Lee, B.-G. Park, and J.-H. Lee, "Multi-layer WSe_2 field effect transistor with improved carrier-injection contact by using oxygen plasma treatment," Solid-State Electronics **140**, 2–7 (2018).
[41]A. Allain and A. Kis, "Electron and hole mobilities in single-layer WSe_2," ACS Nano **8**, 7180–7185 (2014).
[42]J. Rastikian, S. Suffit, S. Timpa, P. Martin, P. Lafarge, O. Bezencenet, M. L. Della Rocca, and C. Barraud, "High performance room temperature p-type injection in few-layered tungsten diselenide films from cobalt and palladium contacts," Mater. Res. Express **6**, 126307 (2019).
[43]M. Kayyalha, J. Maassen, M. Lundstrom, L. Shi, and Y. P. Chen, "Gate-tunable and thickness-dependent electronic and thermoelectric transport in

few-layer MoS_2," J. Appl. Phys. **120**, 134305 (2016).
[44]A. Prakash and J. Appenzeller, "Bandgap extraction and device analysis of ionic liquid gated WSe_2 Schottky barrier transistors," ACS Nano **11**, 1626–1632 (2017).
[45]I. Lee, S. Rathi, L. Li, D. Lim, M. A. Khan, E. S. Kannan, and G.-H. Kim, "Non-degenerate n-type doping by hydrazine treatment in metal work function engineered WSe_2 field-effect transistor," Nanotechnology **26**, 455203 (2015).
[46]H. C. P. Movva, A. Rai, S. Kang, K. Kim, B. Fallahazad, T. Taniguchi, K. Watanabe, E. Tutuc, and S. K. Banerjee, "High-mobility holes in dual-gated WSe_2 field-effect transistors," ACS Nano **9**, 10402–10410 (2015).
[47]N. R. Pradhan, D. Rhodes, S. Memaran, J. M. Poumirol, D. Smirnov, S. Talapatra, S. Feng, N. Perea-Lopez, A. L. Elias, M. Terrones, P. M. Ajayan, and L. Balicas, "Hall and field-effect mobilities in few layered p-WSe_2 field-effect transistors," Sci. Rep. **5**, 2045–2322 (2015).
[48]F. Xia, V. Perebeinos, Y.-m. Lin, Y. Wu, and P. Avouris, "The origins and limits of metal-graphene junction resistance," Nature Nanotechnol. **6**, 179–184 (2011).
[49]C. Kim, I. Moon, D. Lee, M. S. Choi, F. Ahmed, S. Nam, Y. Cho, H.-J. Shin, S. Park, and W. J. Yoo, "Fermi level pinning at electrical metal contacts of monolayer molybdenum dichalcogenides," ACS Nano **11**, 1588–1596 (2017).
[50]D. S. Schulman, A. J. Arnold, and S. Das, "Contact engineering for 2D materials and devices," Chem. Soc. Rev. **47**, 3037–3058 (2018).
[51]S. N. C. Azmi, S. F. A. Rahman, A. Nawabjan, and A. M. Hashim, "Junction properties analysis of silicon back-to-back Schottky diode with reduced graphene oxide Schottky electrodes," Microelectron. Eng. **196**, 32–37 (2018).
[52]J. Kang, W. Liu, D. Sarkar, D. Jena, and K. Banerjee, "Computational study of metal contacts to monolayer transition-metal dichalcogenide semiconductors," Phys. Rev. X **4**, 031005 (2014).
[53]A. Allain, J. Kang, K. Banerjee, and A. Kis, "Electrical contacts to two-dimensional semiconductors," Nature Mater. **14**, 1195–1205 (2015).
[54]C. M. Smyth, L. A. Walsh, P. Bolshakov, M. Catalano, R. Addou, L. Wang, J. Kim, M. J. Kim, C. D. Young, C. L. Hinkle, and R. M. Wallace, "Engineering the palladium–WSe_2 interface chemistry for field effect transistors with high-performance hole contacts," ACS Appl. Nano Mater. **2**, 75–88 (2019).
[55]W. S. Yun, S. W. Han, S. C. Hong, I. G. Kim, and J. D. Lee, "Thickness and strain effects on electronic structures of transition metal dichalcogenides: 2H-MX_2 semiconductors (M = Mo, W; X = S, Se, Te)," Phys. Rev. B **85**, 033305 (2012).
[56]J. Shu, G. Wu, Y. Guo, B. Liu, X. Wei, and Q. Chen, "The intrinsic origin of hysteresis in MoS_2 field effect transistors," Nanoscale **8**, 3049–3056 (2016).
[57]F. Urban, F. Giubileo, A. Grillo, L. Iemmo, G. Luongo, M. Passacantando, T. Foller, L. Madauß, E. Pollmann, M. P. Geller, D. Oing, M. Schleberger, and A. D. Bartolomeo, "Gas dependent hysteresis in MoS_2 field effect transistors," 2D Mater. **6**, 045049 (2019).
[58]Y. Saito, T. Iizuka, T. Koretsune, R. Arita, S. Shimizu, and Y. Iwasa, "Gate-tuned thermoelectric power in black phosphorus," Nano Lett. **16**, 4819–4824 (2016).
[59]A. Laturia, M. L. Van de Put, and W. G. Vandenberghe, "Dielectric properties of hexagonal boron nitride and transition metal dichalcogenides: from monolayer to bulk," NPJ 2D Mater. Appl. **2**, 6 (2018).